IEEE Access
Multidisciplinary | Rapid Review | Open Access Journal

Received April 3, 2021, accepted April 12, 2021, date of publication April 23, 2021, date of current version May 4, 2021.

Digital Object Identifier 10.1109/ACCESS.2021.3075113

Enhancing VTOL Multirotor Performance With a Passive Rotor Tilting Mechanism

IMANOL IRIARTE[1], IÑAKI IGLESIAS[1], JOSEBA LASA[1], HODEI CALVO-SORALUZE[2], AND BASILIO SIERRA[2]

[1]Electric Aircraft Lab by Tecnalia, Basque Research and Technology Alliance (BRTA), 20009 Donostia-San Sebastián, Spain
[2]Robotics and Autonomous Systems Group (RSAIT), University of the Basque Country (UPV-EHU), 20018 Donostia-San Sebastián, Spain

Corresponding author: Imanol Iriarte (imanol.iriarte@tecnalia.com)

This work was supported by the ELKARTEK 2020 Program of the Basque Government under Grant KK-2020/00044.

ABSTRACT This article discusses the benefits of introducing a simple passive mechanism to enable rotor tilting in Vertical Take-Off and Landing (VTOL) multirotor vehicles. Such a system is evaluated in relevant Urban Air Mobility (UAM) passenger transport scenarios such as hovering in wind conditions and overcoming rotor failures. While conventional parallel axis multirotors are underactuated systems, the proposed mechanism makes the vehicle fully actuated in SE(3), which implies independent cabin position and orientation control. An accurate vehicle simulator with realistic parameters is presented to compare in simulation the proposed architecture with a conventional underactuated VTOL vehicle that shares the same physical properties. In order to make fair comparisons, controllers are obtained solving an optimization problem in which the cost function of both systems is chosen to be equivalent. In particular, the control laws are Linear-Quadratic Regulators (LQR), which are derived by linearizing the systems around hover. It is shown through extensive simulation that the introduction of a passive rotor tilting mechanism based on universal joints improves performance metrics such as vehicle stability, power consumption, passenger comfort and position tracking precision in nominal flight conditions and it does not compromise vehicle safety in rotor failure situations.

INDEX TERMS Urban air mobility (UAM), airtaxi, fully actuated vehicle, VTOL, LQR, optimal control, wind gusts, rotor failure, vehicle performance metrics, universal joint.

I. INTRODUCTION

Increasing urban population and rising concerns about atmospheric and acoustic pollution makes it crucial to rethink mobility of goods and people in the city. Urban Air Mobility (UAM) is a recent trend that seeks to leverage the benefits of vertical takeoff and landing (VTOL) vehicles to reduce traffic congestion, commuting times and pollution by taking mobility to the third dimension [1].

Progress in battery technology, microelectromechanical sensors, microprocessors and digital control techniques have recently boosted unmanned aerial vehicles, turning what once was restricted to robotic research labs into a versatile tool with a broad variety of applications such as search and rescue operations, law enforcement, infrastructure inspection, traffic monitoring, agriculture or filming. Micro aerial vehicles have even become a relatively common toy for the wide public.

The associate editor coordinating the review of this manuscript and approving it for publication was Hassen Ouakad.

Driven by such revolution in the access to airspace, many start-ups and large traditional aerospace companies around the world are pursuing the vision of highly automated reduced size aircraft populating urban skies and transporting people in the not so distant future. Most of the proposed concepts and existing prototypes rely on the less noisy and cleaner electric propulsion systems.

Similarly to what happens in today's road traffic, several vehicle architectures are expected to coexist, each fitting a particular objective mission such as intracity air taxi operations, ferry substitutes, touristic attractions, air ambulance operations, airport shuttles or intercity air transport [1]. On the longer range and payload side of the spectrum, winged VTOLs are to be found, with good cruising efficiency. On the contrary, wingless multirotor VTOLs are expected to cover shorter ranges and payloads of one to four passengers, being valued for their maneuverability, hovering efficiency and relatively smaller footprint.

This article is concerned with the latter class of VTOL passenger vehicles. In particular, it aims to explore the implications that the addition of a passive rotor tilting mechanism can have in terms of stability, efficiency, precision, comfort and safety for wingless VTOL vehicles (see Figure 1). The here presented air taxi concept is inspired by a real prototype currently being developed at Tecnalia.

In order to do so, the dynamic response to external events such as wind gusts and rotor failures will be analyzed for a conventional parallel axis multirotor in the spirit of currently existing prototypes such as EHang 216, Volocopter 2X (which actually introduces fixed tilting in its propellers) or CityAirbus, from now on denoted as vehicle architecture A (2a) and a multirotor with the proposed passive rotor tilting mechanism, vehicle architecture B (2b).

A. RELATED WORK

Parallel axis multirotors (also known as collinear multirotors, vehicles where the thrust vector generated by all propellers is oriented in the same direction) are underactuated systems: they cannot simultaneously control their location and orientation. In recent times, aerial robotics community has proposed multiple fully actuated vehicle architectures [2].

Some of the vehicle architectures proposed in the literature achieve full actuation by rotating the propellers with a fixed tilting angle. This is the approach followed by the hexarotors presented in [3]–[6]. The authors of [7]–[9] propose optimizing the propeller position and tilting angle to achieve omnidirectional motion. This procedure of achieving full actuation is mechanically simple but generates energy inefficiencies because part of the thrust produced by the propellers is lost generating internal forces.

Another group of vehicles makes use of dedicated actuators to tilt the propellers. Rotor tilting is simultaneously controlled by means of a single actuator in [10], switching between an underactuated and a fully actuated configuration. However, a more common approach is to actively control the tilting of the propellers, either individually [11]–[13] or collectively [14], [15]. Fully actuated vehicles which rely on dedicated actuators can avoid some of the inefficiencies of fixed tilting vehicles by better aligning thrust, but at the cost of increased system complexity and weight due to the addition of extra actuators.

One last group of fully actuated vehicles consists of collaborative setups where multiple underactuated multirotors are attached to a main body through a passive mechanism providing a way of independently controlling the six degrees of freedom of the central body. Each peripheral underactuated vehicle can be seen as an orientable thrust generator that modifies the control allocation matrix so that any acceleration vector is reachable for the central body. Examples of this approach include cable [16], [17] or spherical joints based systems [18], [19]. The universal joint based architecture presented in [20] lays within this last category and it constitutes the basis for the developments of this article.

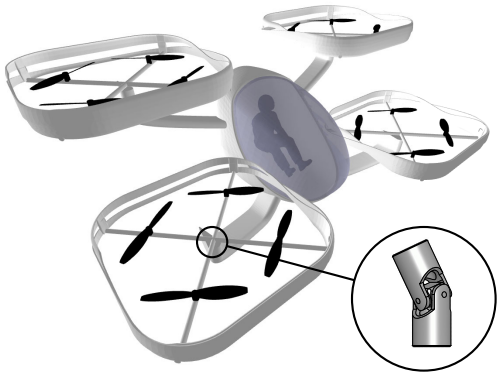

FIGURE 1. Wingless VTOL passenger vehicle with a passive rotor tilting mechanism based on universal joints.

B. CONTRIBUTIONS

This article is a continuation of the work presented in [20], studying the implications of applying such a passive rotor tilting architecture to passenger transport. The main contributions of this article are

- Presentation of an accurate modeling and simulation approach, with a procedure to determine reasonable physical parameters.
- Proposal of an optimization based linear control strategy and selection of cost function parameters to enable a fair comparison between different vehicle architectures.
- Comparison metric definition to analyze vehicle performance in terms of stability, efficiency, precision, comfort and safety.
- Extensive simulation to analyze wind rejection capabilities and resolution of rotor failure situations.

C. STRUCTURE

This document is structured as follows: section II describes the modeling approach followed to characterize the vehicles, as well as the reason behind the choice of all relevant parameters. Section III describes the adopted optimal control strategy and the choice of appropriate cost function parameters to enable a fair comparison, section IV presents extensive simulation results and section V discusses the conclusions of this paper and proposes future research topics.

II. DYNAMIC MODELS

In order to compare in simulation the dynamic behavior of two different vehicle architectures, the first step is to develop a mathematical model of both systems, that determines the evolution of their states under different conditions

$$\dot{\boldsymbol{x}} = \boldsymbol{f}\,(\boldsymbol{x}, \boldsymbol{u}, \boldsymbol{d}) \tag{1}$$

where $\boldsymbol{x}$, $\boldsymbol{u}$ and $\boldsymbol{d}$ are the state, input and disturbance vector, respectively.

Literature is rich presenting dynamic models of parallel axis multirotors, similar to vehicle A (*e.g.* [21]). A derivation of the equations of motion of the vehicle B architecture using Newton-Euler formalism can be found in [20]. Rigid Body Dynamic Algorithms [22] provide a general framework to

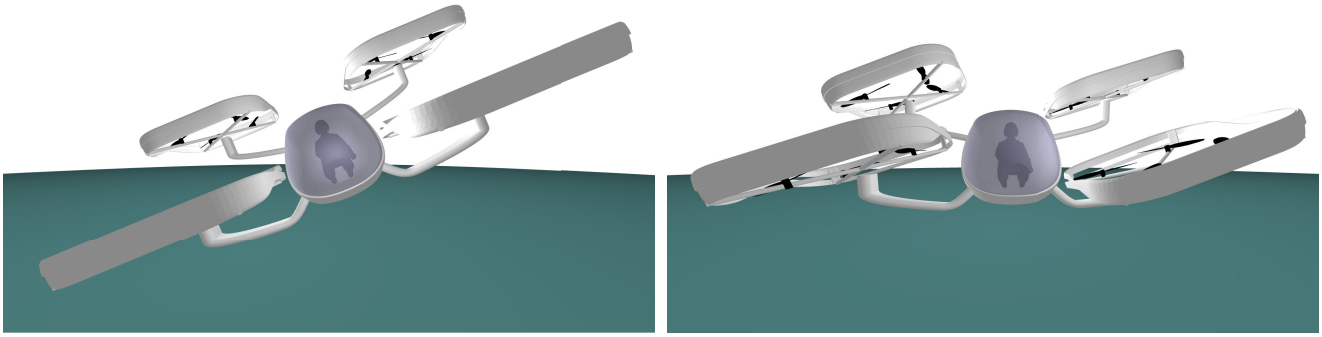

(a) Vehicle architecture A, underactuated (b) Vehicle architecture B, overactuated

FIGURE 2. Reaction to a constant 30 m/s lateral wind speed by the two different models. Parallel axis multirotors are underactuated systems and must sacrifice cabin orientation in order to achieve position control. Full-actuation in SE(3) can be obtained by introducing a simple passive mechanism.

model dynamics of mechanical systems composed of multiple rigid bodies. Taking as an input the inertial properties and kinematic constraints between the different rigid bodies, the algorithms derive efficient code to compute its equations of motion and even perform symbolic operations such as differentiation of the equations.

Modeling and simulation in this work were performed using the implementation of such rigid body algorithms provided by *Drake* [23] and an appropriate visualizer was developed with *MeshCat* [24] (see Figure 2).

A. DEFINITIONS

According to Newton's second law of motion, time invariant mechanical systems can be expressed as second order differential equations of the form

$$\mathbf{M}(\boldsymbol{q}) \cdot \dot{\boldsymbol{v}} = \boldsymbol{f}(\boldsymbol{q}, \boldsymbol{v}, \boldsymbol{u}), \tag{2}$$

where the configuration vector $\boldsymbol{q}$ and the velocity vector $\boldsymbol{v}$ compose the state vector of the system $\boldsymbol{x} = \left[\boldsymbol{q}^{\mathrm{T}}, \boldsymbol{v}^{\mathrm{T}}\right]^{\mathrm{T}}$, $\boldsymbol{u}$ is the input vector and $\mathbf{M}$ is the configuration dependent mass matrix. A system is said to be fully actuated in state $\boldsymbol{x}_0$ if, for every desired value $\dot{\boldsymbol{v}}_d$, there exists a value of $\boldsymbol{u}$ capable of producing such a behavior [25].

The generalized forces acting on the system can be divided into actuation forces $\boldsymbol{f}_a$ which depend on the input vector $\boldsymbol{u}$and not actuated forces $\boldsymbol{f}_{na}$ including Coriolis forces and gravity.

$$\mathbf{M}(\boldsymbol{q}) \cdot \dot{\boldsymbol{v}} = \boldsymbol{f}_{na}(\boldsymbol{q}, \boldsymbol{v}) + \boldsymbol{f}_a(\boldsymbol{q}, \boldsymbol{v}, \boldsymbol{u}), \tag{3}$$

Whenever a dynamic system can be formulated as a control affine expression

$$\boldsymbol{f}_a(\boldsymbol{q}, \boldsymbol{v}, \boldsymbol{u}) = \mathbf{B}(\boldsymbol{q}, \boldsymbol{v}) \cdot \boldsymbol{u}, \tag{4}$$

where $\mathbf{B}$ is the control allocation matrix, the full actuation condition in state $\boldsymbol{x}_0$ can be stated as

$$\operatorname{rank}\{\mathbf{B}(\boldsymbol{x}_0)\} = \dim\{\boldsymbol{v}\}. \tag{5}$$

However, instead of considering full actuation in the entire state space, it is sometimes useful to refer to full actuation in a particular subspace of the system. The configuration space defined by the three dimensional special euclidean group SE(3) is of particular interest, as it includes the six degrees of freedom required to specify the orientation and translation of a rigid body in space [26].

Considering the subset of equations of motion corresponding to translation and rotation,

$$\mathbf{M}^s(\boldsymbol{q}) \cdot \dot{\boldsymbol{v}}^s = \boldsymbol{f}^s_{na}(\boldsymbol{q}, \boldsymbol{v}) + \boldsymbol{f}^s_a(\boldsymbol{q}, \boldsymbol{v}, \boldsymbol{u}), \quad \dot{\boldsymbol{v}}^s \in \mathbb{R}^6 \tag{6}$$

the system is said to be fully actuated in SE(3) in state $\boldsymbol{x}_0$ if for every $\dot{\boldsymbol{v}}^s_d$ there exists a control input $\boldsymbol{u}$ capable of producing such a behavior.

Control input of multirotor aerial vehicles can usually be expressed as $\boldsymbol{u} = [\boldsymbol{u_n}, \boldsymbol{u_\alpha}]^{\mathrm{T}}$, where $\boldsymbol{u_n}$ contains the square of propeller speeds and $\boldsymbol{u_\alpha}$ the control action affecting propeller tilting angles $\boldsymbol{\alpha}$ [2]. Depending on the setup, $\boldsymbol{u_\alpha}$ can consist of a torque, angular speed or directly the tilting angle.

Under such conditions, the SE(3) equations of motion expressed in the vehicle reference frame transform into

$$\mathbf{M}^s(\boldsymbol{q}) \cdot \dot{\boldsymbol{v}}^s = \boldsymbol{f}^s_{na}(\boldsymbol{q}, \boldsymbol{v}) + \mathbf{B}^s(\boldsymbol{\alpha}) \cdot \boldsymbol{u_n}. \tag{7}$$

When propeller tilting angles are fixed ($\dim\{\boldsymbol{u_\alpha}\} = 0$), full actuation in SE(3) can be checked by

$$\operatorname{rank}\left\{\mathbf{B}^s\right\} = 6. \tag{8}$$

When they are not, dynamic full actuation is defined as the existence of a control input trajectory $\boldsymbol{u}(t)$ such that the acceleration trajectory $\dot{\boldsymbol{v}}^s(t)$ converges to any desired value $\dot{\boldsymbol{v}}^s(t) \to \dot{\boldsymbol{v}}^s_d$.

One way of checking the existence of such a trajectory $\boldsymbol{u}(t)$ is by making the following variable transformation

$$\mathbf{B}^s(\boldsymbol{\alpha}) \cdot \boldsymbol{u_n} = \tilde{\mathbf{B}}^s \cdot \tilde{\boldsymbol{u}}(\boldsymbol{u_n}, \boldsymbol{\alpha}), \tag{9}$$

where the new input vector $\tilde{\boldsymbol{u}} = \mathrm{p}(\boldsymbol{u_n}, \boldsymbol{\alpha})$ represents the independently controllable projections of the propeller speed vector. If

$$\operatorname{rank}\left\{\tilde{\mathbf{B}}^s\right\} = 6, \tag{10}$$

there exists a $\tilde{\boldsymbol{u}}$ for every $\dot{\boldsymbol{v}}^s_d$ and the required propeller angular speed $\boldsymbol{u_n}$ and tilting angle $\boldsymbol{\alpha}$ can be retrieved inverting the projection operation $[\boldsymbol{u_n}, \boldsymbol{\alpha}] = \mathrm{p}^{-1}(\tilde{\boldsymbol{u}})$. Thus, if the low level

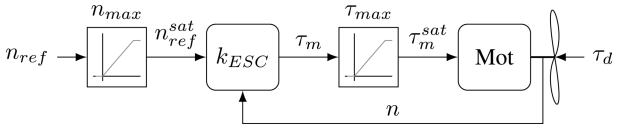

FIGURE 3. Propulsion unit model. Motor speed reference is saturated to the range $n_{ref}^{sat} \in [0, n_{max}]$ and motor torque to the range $\tau_m^{sat} \in [0, \tau_{max}]$.

controllers can find a suitable trajectory of $\boldsymbol{u}_{\boldsymbol{\alpha}}(t)$ to reach the specified $\boldsymbol{\alpha}$, the system is dynamically fully actuated in SE(3).

Systems which do not satisfy the full actuation condition for any state are said to be underactuated systems. On the contrary, systems which satisfy the full actuation condition over a broad region of the state space are commonly referred to as fully actuated systems, even if they can become underactuated in singular configurations or due to actuator or state saturation.

Aerial robotics literature [2] denotes as overactuated the vehicle architectures that besides fulfilling Equation 10, satisfy that

$$\dim\{\boldsymbol{u}\} > \dim\left\{\boldsymbol{\nu}^s\right\} = 6. \tag{11}$$

Thus, the same set of accelerations $\dot{\boldsymbol{\nu}}^s$ can be achieved with different combinations of $\boldsymbol{u}$, which introduces optimality considerations in the control allocation problem. Another subset of fully actuated aerial vehicles are omnidirectional vehicles, which are capable of generating net thrust in any direction regardless of their cabin orientation.

In this sense, vehicle architecture A is underactuated as it does not fulfill Equation 8, whereas B is overactuated (and thus fully actuated) in SE(3). Dynamic full actuation in SE(3) is satisfied because it is possible to independently control net force and torque in the three spatial axes, satisfying Equation 10. Because $\dim\{\tilde{\boldsymbol{u}}\} = 16 > 6$ the vehicle is also overactuated. Besides, being rotor tilting dynamics much faster than cabin dynamics, transient periods to reach $\dot{\boldsymbol{\nu}}_d$ are small. Refer to [20] for more details.

B. VEHICLE DYNAMICS

Both vehicle architectures share a similar structure. The passenger cabin is united by means of rigid arms to four rotor modules M_i, $i = 1, \ldots, 4$. Each of these modules has four propulsion units P_j, $j = 1, \ldots, 4$, composed of a propeller, an electric motor and an *Electronic Speed Controller* (ESC).

Moreover, both vehicle architectures have the same input vector $\boldsymbol{u} \in \mathbb{R}^{16}$ composed by sixteen propeller reference speeds $n_{ref,ij}$; $i = 1, \ldots, 4$; $j = 1, \ldots, 4$. These reference speeds are saturated to $n_{ref}^{sat} \in [0, n_{max}]$ and introduced into an ESC, which is modeled as a sufficiently high proportional gain k_{ESC}. The output of the controller is motor torque τ_m. Motor torque is assumed to always be non-negative, implying that regenerative braking is not considered. Besides, maximum motor torque is limited to τ_{max}, $\tau_m^{sat} \in [0, \tau_{max}]$ (see Figure 3).

Each propeller is assumed to instantaneously generate force and torque proportionally to the square of its angular speed

$$f_{ij} = k_f n_{ij}^2 \tag{12}$$
$$\tau_{ij} = k_\tau n_{ij}^2. \tag{13}$$

Applying Euler's second law of motion to a propulsion unit leads to

$$I_z^P \cdot \dot{n} = \tau_m - \tau_d \tag{14}$$
$$= k_{ESC} \cdot \left(n_{ref} - n\right) - k_\tau \cdot n^2 \tag{15}$$

where τ_m is motor torque, τ_d propeller torque caused by aerodynamic drag, I_z^P the rotational inertia of propeller and rotor and $\dot{n}$ the angular acceleration. Provided that $k_{ESC} \gg k_\tau$, the closed-loop system can be approximated by first-order dynamics (see Figure 6) with time constant and gain

$$\tau = I_z^P / k_{ESC} \quad K_m = 1. \tag{16}$$

The only difference between both architectures is that in vehicle A the modules are rigidly attached to the arms whereas in vehicle B a universal joint is used to connect them. Universal joints introduce two rotational degrees of freedom between each rotor module and the vehicle cabin $\theta_i \in [-\theta_{max}, \theta_{max}]$ and $\phi_i \in [-\phi_{max}, \phi_{max}]$. Joint range limitations are imposed by means of contact constraints in simulation, which turns the model into a hybrid dynamics system, as continuous time dynamics can be altered by a discrete collision event. Universal joints transmit net thrust produced by the rotor modules to the cabin as well as the projection of the net torque vector in axis z_{Ji} (see Figure 4).

Hence, not only system equations are different, but a different state vector is required to describe the motion of each vehicle

$${}^{\mathrm{A}}\dot{\boldsymbol{x}} = {}^{\mathrm{A}}\boldsymbol{f}\left({}^{\mathrm{A}}\boldsymbol{x}, \boldsymbol{u}, \boldsymbol{d}\right) \tag{17}$$
$${}^{\mathrm{B}}\dot{\boldsymbol{x}} = {}^{\mathrm{B}}\boldsymbol{f}\left({}^{\mathrm{B}}\boldsymbol{x}, \boldsymbol{u}, \boldsymbol{d}\right). \tag{18}$$

Vehicle cabin attitude is characterized by means of quaternions, which avoids the singularity of minimum coordinate

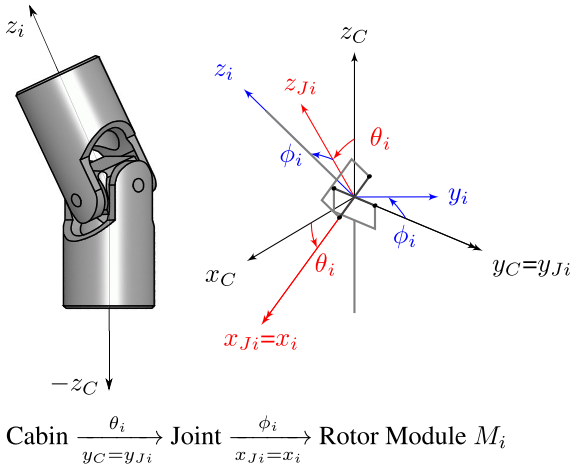

FIGURE 4. Detail of an universal joint and its mathematical representation as two pure rotations. Universal joints transmit forces in every direction and torques along axis z_{Ji}.

TABLE 1. Breakdown of the state vector for the two vehicles.

State Subgroup	Symbol	Vehicle A ${}^{\mathrm{A}}\boldsymbol{x} \in \mathbb{R}^{49}$	Vehicle B ${}^{\mathrm{B}}\boldsymbol{x}^r \in \mathbb{R}^{61}$
Orientation	$\boldsymbol{q}$	q_w q_x q_y q_z	q_w q_x q_y q_z
Position	$\boldsymbol{r}$	r_x r_y r_z	r_x r_y r_z
Rotor Module Orientation	$\boldsymbol{\eta}_i$		$\phi_i, \quad i = 1, \ldots, 4$ $\theta_i, \quad i = 1, \ldots, 4$
Propeller Orientation	$\boldsymbol{\lambda}$	λ_{ij}, $i = 1, \ldots, 4$, $j = 1, \ldots, 4$	λ_{ij}, $i = 1, \ldots, 4$, $j = 1, \ldots, 4$
Angular Speed	$\boldsymbol{\omega}$	ω_x ω_y ω_z	ω_x ω_y ω_z
Linear Speed	$\boldsymbol{v}$	$\dot{r}_x$ $\dot{r}_y$ $\dot{r}_z$	$\dot{r}_x$ $\dot{r}_y$ $\dot{r}_z$
Rotor Module Angular Speed	$\boldsymbol{\omega}_i$		$\omega_{xi}, \quad i = 1, \ldots, 4$ $\omega_{yi}, \quad i = 1, \ldots, 4$
Propeller Speed	$\boldsymbol{n}$	n_{ij}, $i = 1, \ldots, 4$, $j = 1, \ldots, 4$	n_{ij}, $i = 1, \ldots, 4$, $j = 1, \ldots, 4$

representations such as Euler angles. Table 1 shows a detailed description of the state vector for each of the vehicles.

Vehicle dynamic equations are propagated forward in time by means of a variable step third order Runge Kutta integrator. Fast execution is traded off with accuracy with a parameter α as described in [27], such that $\alpha = 10^{-n}$ roughly corresponds to an accuracy of n correct significant digits per result. Simulations in this paper were carried out with a value of $\alpha = 10^{-3}$.

C. REDUCED VEHICLE DYNAMICS

For controller development purposes, it is useful to find a simplified dynamic model of the vehicles with a reduced state vector that captures their essential dynamic behavior

$$\dot{\boldsymbol{x}}^r = \boldsymbol{f}^r\left(\boldsymbol{x}^r, \boldsymbol{u}^r\right). \tag{19}$$

Such a simplified system makes use of ZYX Euler Angles to represent rotations: yaw (ψ), pitch (θ) and roll (ϕ), $\boldsymbol{\eta} = \{\phi, \theta, \psi\}^{\mathrm{T}}$. Even if such a parameterization is not free of singularity, it is useful to linearize the dynamic equations.

Motor dynamics are neglected, assuming that propeller speed can be directly controlled, which leads to a reduced size state vector ${}^{\mathrm{A}}\boldsymbol{x}^r \in \mathbb{R}^{12}$, ${}^{\mathrm{B}}\boldsymbol{x}^r \in \mathbb{R}^{28}$. Besides, propellers are represented as flat, uniform discs with negligible gyroscopic and inertial effects. Taking into consideration Equation 12 and 13, an input variable transformation is carried out

$$u^r_m = u^2_m, \quad m = 1, \ldots, M \tag{20}$$

so that the simplified system can be expressed in a control affine form

$$\dot{\boldsymbol{x}}^r = \boldsymbol{f}^r_{na}\left(\boldsymbol{x}^r\right) + \mathbf{B}\left(\boldsymbol{x}^r\right)\boldsymbol{u}^r. \tag{21}$$

TABLE 2. Commercial propulsion unit taken as reference.

Component	Model
ESC	T-MOTOR FLAME 280A-HV
Motor	T-MOTOR U15L KV43
Propeller	T-MOTOR 47×18 CF

D. PARAMETER SELECTION

Realistic parameters are indispensable for accurate simulation, this is why, whenever possible, commercial components are selected to take parameters from their publicly available technical data sheets. The first step in component selection is the specification of an objective mission for the vehicles. In this case, such an objective is defined as the capability to hover in place with a payload of $m_{pay} = 100\,\mathrm{kg}$ for at least $t_{hov} \geq 15\,\mathrm{min}$, while keeping a thrust to weight ratio of at least $r_{t2w} = 2$ to guarantee maneuverability. Assuming that the mechanical structure, cables and electronics add up to $m_{rest} = 150\,\mathrm{kg}$, the total mass of the vehicle is given by

$$m_T = m_{pay} + m_{bat} + 16 \cdot m_{prop} + m_{rest}, \tag{22}$$

where m_{bat} is the battery mass and m_{prop} is the mass of a propulsion unit composed of ESC, motor and propeller.

Taking for example the product line of the manufacturer *T-Motor*, it can be concluded that a reasonable propeller diameter to achieve the desired thrust to weight ratio is $\varnothing_p = 47\,\mathrm{in}$, with a corresponding battery mass of $m_{bat} = 162\,\mathrm{kg}$ and a total mass of $m_T = 489\,\mathrm{kg}$. Therefore, the commercial components listed in Table 2 are chosen as a reference propulsion unit to determine the vehicle parameters.

The procedure detailed in [28] can be applied to check if the designed system satisfies the objective mission. Propulsion unit manufacturers provide empirical data that relates a set of propeller angular speeds n with other relevant quantities such as generated thrust, torque or consumed current

$$f = f_f(n) \tag{23}$$

$$\tau = f_\tau(n) \tag{24}$$

$$I_e = f_{I_e}(n). \tag{25}$$

Force equilibrium leads to the following hovering condition

$$m_T \cdot \mathrm{g} = N_r \cdot f(n^*), \tag{26}$$

where $n^* = 2217\,\mathrm{rpm} = 232.17\,\mathrm{rad/s}$ is the propeller angular speed required for hover and N_r is the number of rotors.

Assuming a battery pack made of generic lithium ion cells with a specific energy of $\rho_{bat} = 160\,\mathrm{Wh/kg}$ and taking into account the ESC voltage provided by the manufacturer $U_e = 100\,\mathrm{V}$, the total battery charge is

$$C = \frac{m_{bat} \cdot \rho_{bat}}{U_e} = 260\,\mathrm{Ah}. \tag{27}$$

Imposing for safety reasons a minimum charge reserve of 20%, total hover time can be determined

$$t_{hov} = \frac{0.8 \cdot C}{N_r \cdot I_e(n^*)} = 25.2\,\mathrm{min}, \tag{28}$$

where $I_e(n^*) = 31.0\,\mathrm{A}$.

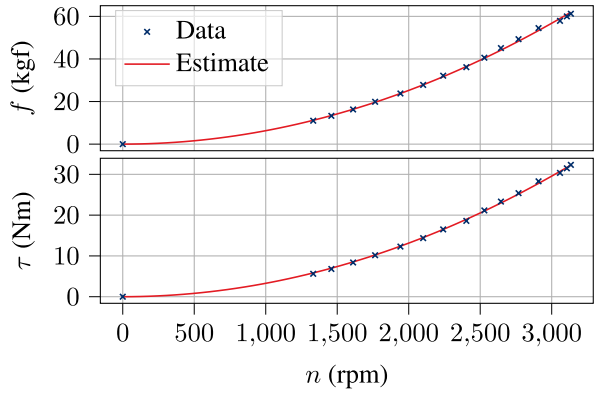

FIGURE 5. Least-Squares parametric estimate of the thrust and torque produced by the chosen propulsion unit.

Defining $\boldsymbol{n} \in \mathbb{R}^{N_{sp}}$ as the vector of angular speed sample points at which the manufacturer provides empirical data and $\boldsymbol{n^2} \in \mathbb{R}^{N_{sp}}$ as the vector satisfying $\boldsymbol{n^2}(i) = \boldsymbol{n}(i)^2, i = 1, \ldots, N_{sp}$. Parameters k_f and k_τ of equations 12 and 13 can be determine from look-up tables 23 and 24 as a Least-Squares problem

$$k_f = \arg\min_{k_f} \left\| f_f(\boldsymbol{n}) - k_f \cdot \boldsymbol{n^2} \right\|_2 \tag{29}$$

$$k_\tau = \arg\min_{k_\tau} \left\| \tau_d(\boldsymbol{n}) - k_\tau \cdot \boldsymbol{n^2} \right\|_2 \tag{30}$$

with a well-known closed form solution.

$$k_f = \boldsymbol{n^2}^\dagger \cdot f_f(\boldsymbol{n}), \quad k_\tau = \boldsymbol{n^2}^\dagger \cdot \tau_d(\boldsymbol{n}) \tag{31}$$

where $\boldsymbol{n^2}^\dagger$ denotes the pseudo-inverse of $\boldsymbol{n^2}$

$$\boldsymbol{n^2}^\dagger = \left(\boldsymbol{n^2}^{\mathrm{T}} \cdot \boldsymbol{n^2}\right)^{-1} \cdot \boldsymbol{n^2}^{\mathrm{T}}. \tag{32}$$

The results of such an estimation for the chosen components can be seen in Figure 5, where

$$k_f = 5.64 \cdot 10^{-3}\,\mathrm{N{\cdot}s^2}, \quad k_\tau = 3.00 \cdot 10^{-4}\,\mathrm{Nm{\cdot}s^2}. \tag{33}$$

The selected motor has a velocity constant of $k_v = 43\,\mathrm{rpm\,/\,V}$ and a peak current of $I_{max} = 160\,\mathrm{A}$ for 120 s. Maximum torque is derived from those quantities with

$$\tau_{max} = \frac{I_{max}}{k_v}. \tag{34}$$

Which corresponds with a maximum torque of $\tau_{max} = 66\,\mathrm{Nm}$. Maximum commanded speed is taken from manufacturer tables at full throttle $n_{max} = 3113\,\mathrm{rpm} = 326.08\,\mathrm{rad/s}$.

The determination of inertial parameters of the vehicle is performed with the help of CAD software where the vehicle geometry and material (mainly composite materials) are specified. Passenger inertial properties are taken from [29] and extra payload is assumed to be a homogeneous cube of 40 cm. All inertia is considered to be referenced to the center of mass of each body and expressed in their principal axes of inertia which, assuming symmetry, implies that only diagonal inertia matrices are considered. Inertia is grouped in three rigid bodies: the cabin (including arms, passenger, payload and battery), the rotor modules (including ESCs and motors) and the propellers. Resulting values are detailed in Table 3.

TABLE 3. Chosen inertia parameters.

	Ixx (kg m^2)	Iyy (kg m^2)	Izz (kg m^2)
Cabin	$1.76 \cdot 10^2$	$1.26 \cdot 10^2$	$1.40 \cdot 10^2$
Module	9.25	9.25	18.07
Propeller	$8.01 \cdot 10^{-4}$	$4.01 \cdot 10^{-2}$	$4.07 \cdot 10^{-2}$

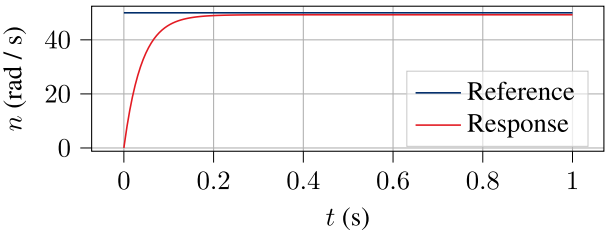

FIGURE 6. Step response of the propulsion unit can be characterized as a first order system with time constant $\tau = 40\,\mathrm{ms}$.

TABLE 4. Values of area and drag coefficient in each axis.

Axis	x	y	z
$A\,(\mathrm{m}^2)$	3.97	4.94	5.43
C_D	0.45	0.50	0.55

With those inertial parameters, Equation 16 shows that choosing $k_{ESC} = 1$ is leads to a first-order dynamic response with time constant $\tau = 40\,\mathrm{ms}$ (see Figure 6), which is fast enough to provide good control, while avoiding stiffness issues and power spikes.

The separation between rotor module attaching points is $\Delta x = 1\,\mathrm{m}$, $\Delta y = 2.16\,\mathrm{m}$, $\Delta z = 0.72\,\mathrm{m}$ and propellers have a separation of $\Delta r = 1.2\,\mathrm{m}$ inside the module. Universal joint range is limited to $\phi_{max} = \theta_{max} = 45°$.

E. WIND MODEL

An effective way to test the performance of the two vehicle architectures is to analyze their reaction to wind disturbances. Wind speed exerts aerodynamic forces such that

$$F_{w_i} = \frac{1}{2} \cdot \rho_a \cdot C_{Di} \cdot A_i \cdot {v_{w_i}}^2, \quad i = x, y, z \tag{35}$$

where $\rho_a = 1.225\,\mathrm{kg\,/\,m^3}$ is the air density at the sea level and 15 °C, C_{Di} is the drag coefficient of each axis, A_i is the projected area of the vehicle and v_{wi} is the wind speed. Some values for the vehicles of this study are proposed in Table 4.

Wind speed can be divided in two components: turbulence and gusts. Turbulence causes random but correlated variations in wind speed and it can be efficiently modeled as a stochastic process. Wind gusts constitute a sudden coherent variation of wind speed in a definite direction [30].

Traditionally, turbulence modeling for large aircraft traveling at high speed has been performed by means of the Dryden and Von Kármán stochastic models, which define a specific power spectrum that realistically matches the frequency content of wind at such conditions. However, [31] proposes a simpler approach to model wind turbulence at low altitudes and speeds by filtering white Gaussian noise with a first order low-pass filter, what is known as a first order Gauss-Markov

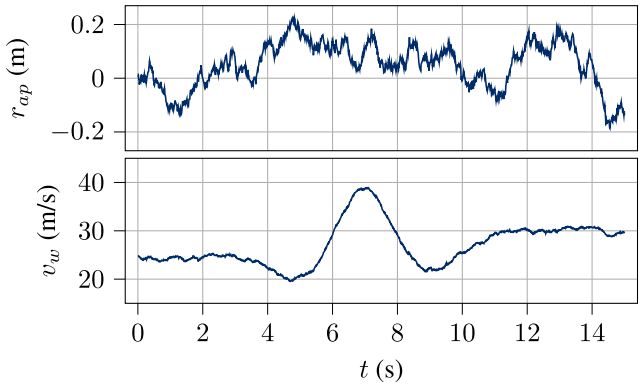

FIGURE 7. Example of simulated wind force application point and wind velocity curves with $A_g = 25$ m/s.

process

$$\dot{v}^t_{w_i} = -a_i \cdot v^t_{w_i} + b_i \cdot w_i, \quad i = x, y, z \tag{36}$$

where w_i is a zero mean and unit covariance white Gaussian noise. Equation 36 corresponds to a first order transfer function with time constant and gain

$$\tau_{w_i} = 1/a_i, \quad K_{w_i} = b_i/a_i, \ i = x, y, z. \tag{37}$$

While turbulence generates realistic conditions to test the controllers, the goal of this investigation is to analyze the behavior of two vehicle architectures in windy environments of different severity. Such an environment can be simulated by means of wind gusts of varying amplitude. Wind gusts are modeled with the analytical expression proposed in [32] for extreme operating gusts, which provides a characteristic symmetric gust shape

$$v^g_w = -\Delta v_g \sin\left(3\pi \frac{t}{t_g}\right)\left(1 - \cos\left(2\pi \frac{t}{t_g}\right)\right), \quad 0 < t < t_g \tag{38}$$

where Δv_g is the relative gust amplitude, which can be approximately correlated to mean wind speed by

$$\Delta v_g = 0.25 \cdot v^m_w \tag{39}$$

and t_g is the total gust duration, which is linearly correlated to the relative gust amplitude

$$t_g = 0.71 \cdot \Delta v_g + 3.51. \tag{40}$$

Wind gusts are assumed to affect exclusively the horizontal plane, with random direction.

Total wind speed is computed by adding turbulence, gusts and wind mean speed

$$\boldsymbol{v_w} = \boldsymbol{v_w}^t + \boldsymbol{v_w}^g + \boldsymbol{v_w}^m \tag{41}$$

and the force application point is assumed to also vary as a first order Gauss-Markov process around the center of mass of the vehicle, with time constant τ_{ap} and gain K_{ap}, leading to the exertion of not only force, but also net angular moment.

States corresponding to wind turbulence and force application point are initialized $x_0 = 0$ at the beginning of every simulation episode and are integrated forward in time by means of the explicit Euler procedure, with a fixed sample-time of $\Delta T = 10$ ms.

Simulations are performed considering a total gust episode duration of $t_e = 15$ s. According to Beaufort wind scale, wind speeds of over 32 m / s are present in hurricanes. Thus, present simulations consider mean wind speed variations in a range $v^m_w \in 0 - 30$ m / s. Parameters corresponding to the dynamics of wind turbulence and wind application point are set to $K_t = 100$, $\tau_t = 10$, $K_{ap} = 20$, $\tau_{ap} = 20$. Such a combination leads to random wind speed and application point patterns like the ones shown in Figure 7.

III. CONTROL

In order to make a fair performance comparison of two similar but different vehicle architectures, an equivalent control law is required, so that none of the vehicles is penalized due to its control algorithm. One way of achieving such an equivalence is making use of optimal control strategies [33], where the control designer only has to specify a general structure of the controller and some high-level performance criterion (a cost function) and the details of the control algorithm are left to numerical optimization.

A. LINEAR-QUADRATIC REGULATOR (LQR)

A particularly simple optimal control algorithm is the Linear-Quadratic Regulator (LQR), which corresponds to the optimal linear controller when the system of choice is linear and the cost function is quadratic. Even if these conditions are quite restrictive, it is possible to approach many nonlinear systems of the form

$$\dot{\boldsymbol{x}} = \boldsymbol{f}(\boldsymbol{x}, \boldsymbol{u}) \tag{42}$$

by their linear approximation making a first order Taylor expansion around an equilibrium point $\boldsymbol{x_0}$, such that $\boldsymbol{f}(\boldsymbol{x_0}, \boldsymbol{u_0}) = 0$.

$$\dot{\boldsymbol{x}} \approx \left.\frac{\partial \boldsymbol{f}(\boldsymbol{x}, \boldsymbol{u})}{\partial x}\right|_{\boldsymbol{x_0}, \boldsymbol{u_0}} (\boldsymbol{x} - \boldsymbol{x_0}) + \left.\frac{\partial \boldsymbol{f}(\boldsymbol{x}, \boldsymbol{u})}{\partial u}\right|_{\boldsymbol{x_0}, \boldsymbol{u_0}} (\boldsymbol{u} - \boldsymbol{u_0}) \tag{43}$$

Which can be converted to the standard linear state-space form

$$\dot{\bar{\boldsymbol{x}}} = \mathbf{A}\bar{\boldsymbol{x}} + \mathbf{B}\bar{\boldsymbol{u}}. \tag{44}$$

A frequent objective in controller development is to stabilize the system around an equilibrium point, making use of limited control effort. This goal can be expressed with a quadratic cost function

$$J = \int_0^\infty \left(\bar{\boldsymbol{x}}^{\mathrm{T}}\mathbf{Q}\bar{\boldsymbol{x}} + \bar{\boldsymbol{u}}^{\mathrm{T}}\mathbf{R}\bar{\boldsymbol{u}}\right) dt, \tag{45}$$

where $\mathbf{Q}$ is a symmetric positive semidefinite matrix that weights the cost associated to each state and $\mathbf{R}$ is a symmetric positive definite matrix that weights the cost of each control action.

The optimal cost-to-go function $J^*(\bar{\boldsymbol{x}})$ for a linear system with a quadratic cost function is known to also be quadratic [25]

$$J^*(\bar{\boldsymbol{x}}) = \bar{\boldsymbol{x}}^{\mathrm{T}}\mathbf{S}\bar{\boldsymbol{x}}, \tag{46}$$

with $\mathbf{S}$ symmetric positive semidefinite. Both optimal cost-to-go function $J^*(\bar{\boldsymbol{x}})$ and optimal policy $\bar{\boldsymbol{u}}^*$ of the controller must satisfy the Hamilton-Jacobi-Bellman (HJB) equation [33] and, when the system is controllable, this leads to an optimal policy of the form

$$\bar{\boldsymbol{u}}^* = -\mathbf{R}^{-1}\mathbf{B}^{\mathrm{T}}\mathbf{S}\bar{\boldsymbol{x}} = -\mathbf{K}\bar{\boldsymbol{x}}. \tag{47}$$

When the LQR problem is formulated as an infinite horizon continuous-time problem, the matrix $\mathbf{S}$ can be determined by solving a continuous-time algebraic Riccati equation

$$0 = \mathbf{SA} + \mathbf{A}^{\mathrm{T}}\mathbf{S} - \mathbf{SBR}^{-1}\mathbf{B}^{\mathrm{T}}\mathbf{S} + \mathbf{Q}. \tag{48}$$

Thus, the optimal controller gain matrix $\mathbf{K}$ can be conveniently computed offline, finding an explicit expression for the optimal control law

$$\boldsymbol{u}^* = \boldsymbol{u_0} - \mathbf{K}\left(\boldsymbol{x} - \boldsymbol{x_0}\right). \tag{49}$$

Applying the LQR controller to nonlinear systems like Equation 42 does not yield optimal results all over the state-space, but it provides a very computationally efficient algorithm to stabilize the system around a region of attraction of the equilibrium point.

A simple way of making the LQR algorithm robust against system uncertainty and unmodeled phenomena is the inclusion of integral terms. However, the goal of this exercise is to compare the performance of two architectures in the same conditions, therefore, no integrator is introduced to minimize complexity.

B. LQR COST COEFFICIENT SELECTION

Determining a set of coefficients for matrices $\mathbf{Q}$ and $\mathbf{R}$ is not a trivial task. The number of free parameters to tune controllers for both vehicles adds up to 756. These parameters should provide to the controller information about the relative importance of each state and control signal in the overall control problem, taking into account the units in which each magnitude is expressed. Depending on the chosen coefficients, the vehicle performance can vary significantly. Thus, it is required to find a set of reasonable coefficients that leads to a fair comparison between the two vehicle architectures.

Whenever there is not any particularly strong penalty associated with simultaneously having error in a combination of states or with making simultaneous use of a set of actuators, it is common practice to neglect the non-diagonal elements of both matrices, which ostensibly reduces the set of free parameters to 72.

$$\mathbf{Q} = \begin{bmatrix} q_1 & 0 & 0 \\ 0 & \ddots & 0 \\ 0 & 0 & q_N \end{bmatrix}, \quad \mathbf{R} = \begin{bmatrix} r_1 & 0 & 0 \\ 0 & \ddots & 0 \\ 0 & 0 & r_M \end{bmatrix} \tag{50}$$

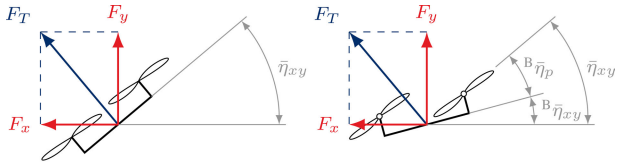

FIGURE 8. Bidimensional schematic representation of the correction mechanisms of both vehicle architectures. In order to produce the same net rotor inclination $\bar{\eta}_{xy}$ vehicle A orientates the whole cabin $^{\mathrm{A}}\bar{\eta}_{xy}$ while vehicle B can either orientate the cabin $^{\mathrm{B}}\bar{\eta}_{xy}$ or the propellers with respect to the cabin $^{\mathrm{B}}\bar{\eta}_p$.

A simple procedure to find reasonable parameters was proposed by Bryson [34]. The idea is that the control designer should specify "*acceptable*" deviations from equilibrium for each state $\bar{x}_n^a$ and control action $\bar{u}_m^a$, which are, based on knowledge of the system, considered to be equivalently pernicious for the control performance. Then, each cost coefficient can be chosen so that the following conditions are met

$$q_n \cdot (\bar{x}_n^a)^2 = 1 \quad n = 1, \ldots, N \tag{51}$$
$$r_m \cdot (\bar{u}_m^a)^2 = 1 \quad m = 1, \ldots, M \tag{52}$$

Because the systems studied in this work exclusively have one type of actuators, we establish as reasonable that

$$r_m = r = 1/(\bar{u}^a)^2 \quad m = 1, \ldots, M \tag{53}$$

Taking horizontal symmetry into consideration, it is possible to reduce the number of free parameters by aggregating horizontal translational and rotational states in more general categories. This leads to the following set of 20 parameters, to be determined by the controller designer:

$$^{\mathrm{A}}\bar{u}^a \; ^{\mathrm{A}}\bar{\eta}_{xy}^a \; ^{\mathrm{A}}\bar{\psi}^a \; ^{\mathrm{A}}\bar{r}_{xy}^a \; ^{\mathrm{A}}\bar{r}_z^a \; ^{\mathrm{A}}\bar{\omega}_{xy}^a \; ^{\mathrm{A}}\bar{\omega}_z^a \; ^{\mathrm{A}}\bar{v}_{xy}^a \; ^{\mathrm{A}}\bar{v}_z^a$$
$$^{\mathrm{B}}\bar{u}^a \; ^{\mathrm{B}}\bar{\eta}_{xy}^a \; ^{\mathrm{B}}\bar{\psi}^a \; ^{\mathrm{B}}\bar{r}_{xy}^a \; ^{\mathrm{B}}\bar{r}_z^a \; ^{\mathrm{B}}\bar{\eta}_p^a \; ^{\mathrm{B}}\bar{\omega}_{xy}^a \; ^{\mathrm{B}}\bar{\omega}_z^a \; ^{\mathrm{B}}\bar{v}_{xy}^a \; ^{\mathrm{B}}\bar{v}_z^a \; ^{\mathrm{B}}\bar{\omega}_p^a$$

However, in order to make both models comparable, some relationships must be satisfied by the parameters of both vehicle models, so that they assign costs equivalently.

$$\bar{u}^a = {}^{\mathrm{A}}\bar{u}^a = {}^{\mathrm{B}}\bar{u}^a \tag{54}$$
$$\bar{r}_{xy}^a = {}^{\mathrm{A}}\bar{r}_{xy}^a = {}^{\mathrm{B}}\bar{r}_{xy}^a \tag{55}$$
$$\bar{r}_z^a = {}^{\mathrm{A}}\bar{r}_z^a = {}^{\mathrm{B}}\bar{r}_z^a \tag{56}$$
$$\bar{v}_{xy}^a = {}^{\mathrm{A}}\bar{v}_{xy}^a = {}^{\mathrm{B}}\bar{v}_{xy}^a \tag{57}$$
$$\bar{v}_z^a = {}^{\mathrm{A}}\bar{v}_z^a = {}^{\mathrm{B}}\bar{v}_z^a \tag{58}$$
$$\bar{\eta}_{xy}^a = {}^{\mathrm{A}}\bar{\eta}_{xy}^a = {}^{\mathrm{B}}\bar{\eta}_{xy}^a + {}^{\mathrm{B}}\bar{\eta}_p^a \tag{59}$$
$$\bar{\psi}^a = {}^{\mathrm{A}}\bar{\psi}^a = {}^{\mathrm{B}}\bar{\psi}^a \tag{60}$$
$$\bar{\omega}_{xy}^a = {}^{\mathrm{A}}\bar{\omega}_{xy}^a = {}^{\mathrm{B}}\bar{\omega}_{xy}^a + {}^{\mathrm{B}}\bar{\omega}_p^a \tag{61}$$
$$\bar{\omega}_z^a = {}^{\mathrm{A}}\bar{\omega}_z^a = {}^{\mathrm{B}}\bar{\omega}_z^a \tag{62}$$

The rationale behind Equation 59 and 61 is that, in both systems, the horizontal translational error is tightly related with the total orientation of the rotors. While model A can only increase $^{\mathrm{A}}\bar{\eta}_{xy}$ to produce a given horizontal force, model B can produce the same force by combining $^{\mathrm{B}}\bar{\eta}_{xy}$ with $^{\mathrm{B}}\bar{\eta}_p$ (see Figure 8).

TABLE 5. Free parameters.

Positions	Velocities	Actuation
$\bar{\eta}^a_{xy}$	$\bar{\omega}^a_{xy}$	
${}^{\mathrm{B}}\bar{\eta}^a_{xy}$	${}^{\mathrm{B}}\bar{\omega}^a_{xy}$	
$\bar{\psi}^a$	$\bar{\omega}^a_z$	$\bar{u}^a$
$\bar{r}^a_{xy}$	$\bar{v}^a_{xy}$	
$\bar{r}^a_z$	$\bar{v}^a_z$	

Equations 54 to 62 reduce the size of the independent parameter space to a total of 11 free parameters, which can be grouped under the labels of positions, velocities and actuation (see Table 5).

Considering Equation 47 and 48, one can infer that there exist infinite pair of matrices $\mathbf{Q}' = a \cdot \mathbf{Q}$, $\mathbf{R}' = a \cdot \mathbf{R}$ such that $\mathbf{S}' = a \cdot \mathbf{S}$, making the controller gain $\mathbf{K}$ remain the same. In other words, scaling every free parameter by the same constant would leave the resulting controller unchanged.

Having all these elements into consideration, the coefficient selection process is started by specifying position coefficients. Given extensive simulation experience, we propose the following values as reasonable:

$$\bar{\eta}^a_{xy} = 30°,\ {}^{\mathrm{B}}\bar{\eta}^a_{xy} = 0.1°,\ \bar{\psi}^a = 0.5°,$$
$$\bar{r}^a_{xy} = 0.1\,\mathrm{m},\ \bar{r}^a_z = 0.01\,\mathrm{m}$$

Due to the nature of these systems, tight precision requirements in the horizontal plane (low $\bar{r}^a_{xy}$) require relatively large values of total rotor inclination $\bar{\eta}^a_{xy}$. The choice of ${}^{\mathrm{B}}\bar{\eta}^a_{xy} \ll \bar{\eta}^a_{xy}$ was performed to encourage the relative motion between rotors and cabin in model B, stressing out the differences between models (Figure 8). A small $\bar{r}^a_z$ is required to compensate the lack of integrator and guarantee reasonable height tracking.

Similarly, the following maximum admissible velocity deviations are proposed:

$$\bar{\omega}^a_{xy} = 30\ °/\mathrm{s},\ {}^{\mathrm{B}}\bar{\omega}^a_{xy} = 0.1\ °/\mathrm{s},\ \bar{\omega}^a_z = 0.5\ °/\mathrm{s},$$
$$\bar{v}^a_{xy} = 0.1\,\mathrm{m/s},\ \bar{v}^a_z = 0.01\,\mathrm{m/s}$$

Given from subsection II-D that $u_0 = 232.17\,\mathrm{rad/s}$ and $u_{max} = 326.08\,\mathrm{rad/s}$ we consider that a reasonable deviation of the control action for the level of state error proposed is

$$\bar{u}^a = 50\,\mathrm{rad/s}.$$

These values are the nominal coefficients chosen for the comparison, however, in order to test the vehicles under a broader variety of conditions, two other sets of parameters will be tested, loosening and tightening the displacement tracking requirements to vary the responsiveness of the controllers. A detailed list can be found in Table 6.

IV. RESULTS

In the following section, the performance of both vehicle architectures is compared in terms of stability, precision, comfort and efficiency for different wind conditions and controller cost functions by means of extensive simulation. Besides, safety is addressed simulating a rotor failure scenario. All tests are conducted in hover, at the linearization point used for LQR controller development. A video summary of the here presented results can be found in the supplementary material and in the link referenced in the abstract.

TABLE 6. Summary of chosen cost coefficients.

set	$\bar{\eta}^a_{xy}$ (°)	${}^{\mathrm{B}}\bar{\eta}^a_{xy}$ (°)	$\bar{\psi}^a$ (°)	$\bar{r}^a_{xy}$ (m)	$\bar{r}^a_z$ (m)	$\bar{\omega}^a_{xy}$ (°/s)	${}^{\mathrm{B}}\bar{\omega}^a_{xy}$ (°/s)	$\bar{\omega}^a_z$ (°/s)	$\bar{v}^a_{xy}$ (m/s)	$\bar{v}^a_z$ (m/s)	$\bar{u}^a$ (rad/s)
Loose	30	0.1	1	0.5	0.01	30	0.1	0.5	0.1	0.01	50
Nominal	30	0.1	0.5	0.1	0.01	30	0.1	0.5	0.1	0.01	50
Tight	30	0.1	0.05	0.01	0.01	30	0.1	0.5	0.1	0.01	50

A. WIND DISTURBANCES

Figure 9 shows the simulated reaction of model A and B to windy conditions like the ones described in subsection II-E. While both vehicles have equivalent controllers (see subsection III-B), the response as perceived in the cabin is very different: because of its full actuation in SE(3), vehicle B requires minimum cabin oscillations to overcome the gust and displacement error is smaller too.

Due to the randomness of wind models, extensive simulation is required to make general statements. Thus, in order to analyze the vehicle response to different wind gust amplitudes, each episode of $t_e = 15\,\mathrm{s}$ is simulated $N_e = 500$ times for each vehicle at each value of mean wind speed in the range $v^m_w \in [0, 30]\,\mathrm{m/s}$.

At each episode, the following performance metrics are collected:

- **Stability percentage:** The percentage of episodes where the vehicle remains stable in hover conditions

$$\rho_s = \frac{N_s}{N_e}. \tag{63}$$

  An episode is considered unstable when the center of mass presents a divergence from its reference position greater or equal to 15 m (for loose state tracking parameters it is increased to 20 m) or the cabin roll or pitch exceed $\pi/2$ rad.
- **Mean power consumption:** Episodic mean of the mechanical power required to maintain hover, it provides information about the efficiency of each vehicle

$$P_m = \frac{\int_0^{t_e} \left(\boldsymbol{n}^{\mathrm{T}} \cdot \boldsymbol{\tau}\right) \mathrm{d}t}{t_e}, \tag{64}$$

  where $\boldsymbol{n}$ is the vector of propeller speeds and $\boldsymbol{\tau}$ is the vector of motor torques. This magnitude is averaged between the amount of episodes in which both vehicles were stable N^*_s

$$P^*_m = \frac{\sum_{i=1}^{N^*_s} P_{m_i}}{N^*_s}. \tag{65}$$

- **Maximum translation error:** Maximum deviation of the linear position coordinates inside an episode, it is related with the safety distance required around the vehicle.

$$\hat{r}_{xy} = \left\| r_{xy} \right\|_\infty, \tag{66}$$
$$\hat{r}_z = \left\| r_z - r_{z_0} \right\|_\infty \tag{67}$$

where r_{xy} is the total horizontal displacement computed as

$$r_{xy} = \sqrt{r_x^2 + r_y^2}. \tag{68}$$

This magnitudes are averaged between the amount of episodes where both vehicles where stable N_s^*

$$\hat{r}_i^* = \frac{\sum_{i=1}^{N_s^*} \hat{r}_i}{N_s^*}, \quad i = xy, z. \tag{69}$$

- **Maximum angular error:** Maximum deviation of the angular position coordinates inside an episode, it is a proxy of passenger comfort. While passenger comfort is a subjective magnitude, influenced by many factors, large angular variations are assumed to be correlated with greater passenger discomfort and feeling of danger.

$$\hat{\eta}_{xy} = \left\| \eta_{xy} \right\|_\infty \tag{70}$$

$$\hat{\eta}_z = \left\| \eta_z - \eta_{z_0} \right\|_\infty \tag{71}$$

where $\eta_z = \psi$ and η_{xy} is the total horizontal rotation computed as

$$\eta_{xy} = \operatorname{acos}(\cos\phi \cdot \cos\theta) \tag{72}$$

and it corresponds to the total angle between the reference axis z_0 and the z_B axis attached to the vehicle cabin. This magnitudes are averaged between the amount of episodes where both vehicles were stable N_s^*

$$\hat{\eta}_i^* = \frac{\sum_{i=1}^{N_s^*} \hat{\eta}_i}{N_s^*}, \quad i = xy, z. \tag{73}$$

Figure 10 shows simulation results for each of the three controller cost coefficients of Table 6. Each graph required simulating 14.6 h of flight per vehicle.

10b shows the behavior of both vehicles with controllers optimized for the nominal cost coefficient set (see Table 6). When wind speeds are low, both vehicle architectures behave similarly. However, as wind speed passes the threshold of 10 m/s, model A percentage stability decreases to 92.36 %, reaching 26.2 % for a mean wind speed of 30 m/s. Model B shows better stability properties and it can reach as much as 99.8 % stability for a mean wind speed of 30 m/s.

Such a behavior is explainable because the LQR controller can only stabilize the system around a region of attraction where the linearization assumptions hold. Vehicle A is more easily forced out of that region of attraction because it has to move a larger inertia to orientate the net thrust vector and is therefore slower. Besides, vehicle model A has a lower yaw control authority, because it must correct yaw deviations exclusively with propeller torque, whereas vehicle model B can combine it with thrust vectoring strategies.

Power consumption is very similar in both vehicles when wind speed is low. As wind speed increases, energy consumption increases in vehicle A, reaching up to 5.8 % more for a mean wind speed of 30 m/s. Once again, such a behavior can be attributed to the larger inertia and lower yaw control authority of vehicle model A.

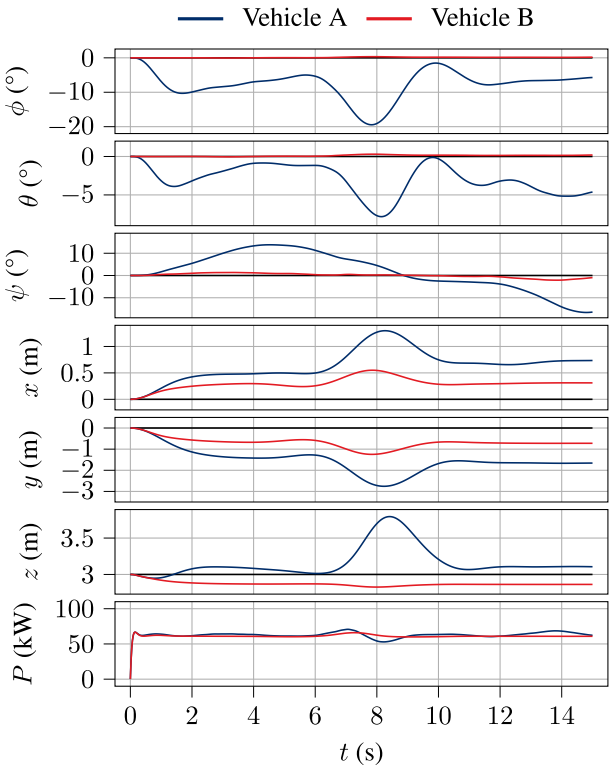

FIGURE 9. Cabin states reacting to a wind gust with $v_g^m = 25$ m/s and nominal controller parameter set.

For the same reasons, horizontal displacement error reaches 4.0 m in vehicle A and 2.0 m in vehicle B and vertical error in vehicle A is 1.2 m whereas in vehicle B it is 0.2 m for wind speeds of 30 m/s.

Regarding angular error, horizontal angular error is up to an order of magnitude larger in vehicle A, which is reasonable due to its underactuation, it is not physically possible to minimize translation error without sacrificing pitch and roll. It is remarkable however the large error in yaw angle of vehicle A in comparison with vehicle B for high wind speeds which can once again be attributed to the previously mentioned reduced yaw control authority.

Loose position tracking coefficients are tested in 10a. The effect of loosening position tracking is that stability is slightly increased and power consumption slightly decreased, but at the cost of substantially increasing translation and yaw error. 10c shows tight position tracking coefficients which lead to very reactive controllers. Such controllers significantly reduce position error at the cost of decreasing vehicle stability.

As a general conclusion, making use of controllers optimized against different cost functions, vehicle architecture B shows a more stable behavior and it achieves similar or less displacement error with less energy consumption and drastically less variations in cabin orientation. It must be remarked that these results were obtained for short episodes ($t_e = 15$ s) and hovering conditions. Longer gusts could affect mean consumed power and position error could be reduced introducing integral terms in the controller. Besides, following a cruising

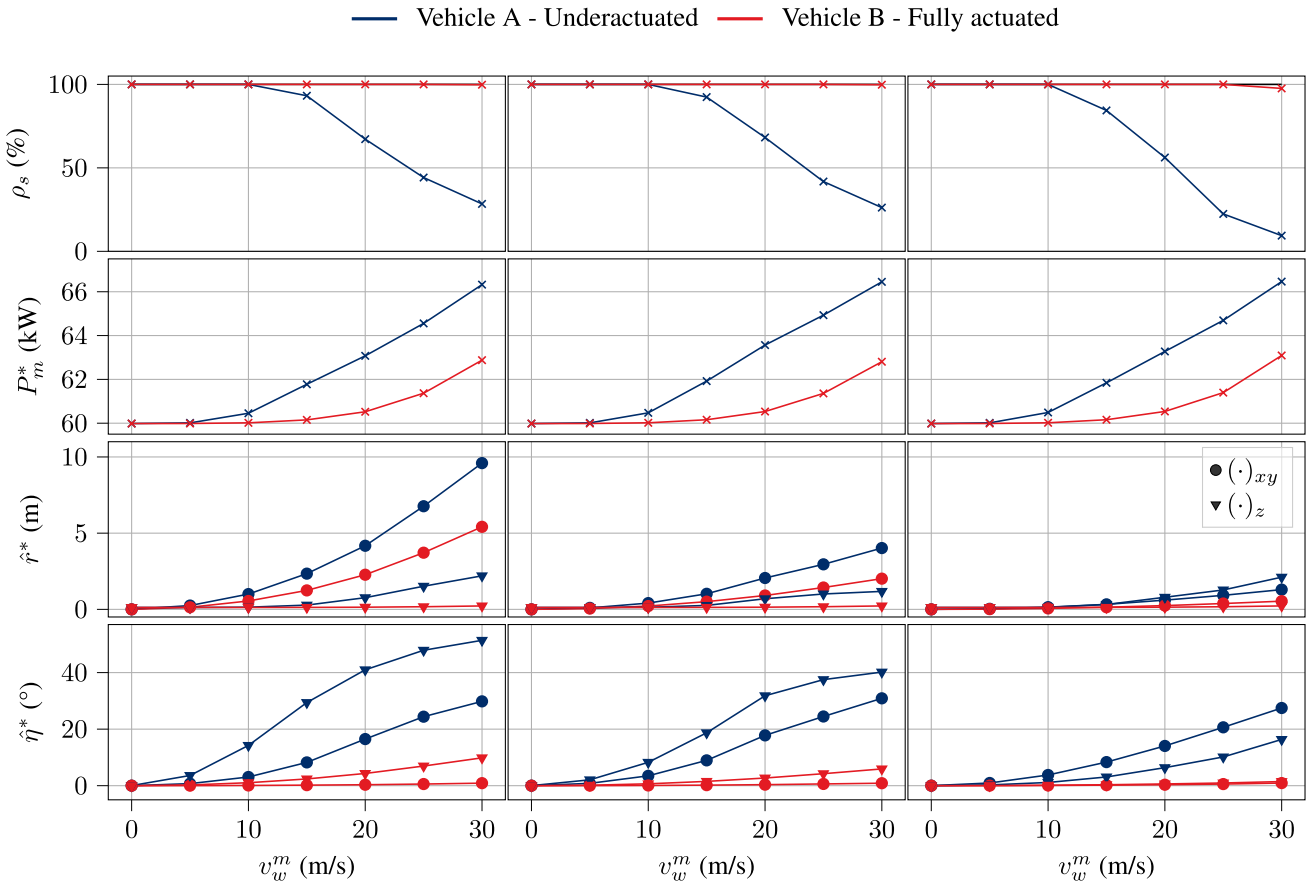

(a) Loose state tracking requirements. (b) Nominal state tracking requirements. (c) Tight state tracking requirements.

FIGURE 10. Wind rejection performance metrics of the two vehicle architectures for different wind gust amplitudes and controller parameter sets. Every point is averaged over the stable proportion of $N_e = 500$ episodes.

trajectory instead of hovering could also affect the power consumption characteristics of the vehicles, as vehicle model B could keep the cabin in its minimum drag orientation. However, the goal of this exercise is to compare the metrics of both architectures under the same conditions, everything else being equal. The here presented simulations enable to conclude that wind rejection capabilities can be improved by means of the proposed passive rotor tilting mechanism.

B. ROTOR FAILURE

Even if vehicle architecture B shows good properties in nominal operation mode, a reasonable concern is its ability to deal with catastrophic events such as a propeller or motor loss. While quadrotors must sacrifice control of a degree of freedom when a rotor fails [35], multirotors are well known for the robustness provided by their redundant propulsion system which allows them to perform a safe emergency landing when a propulsion unit is lost [36].

In order to test the behavior of both vehicles when a rotor failure happens, the LQR controllers developed in section III are employed with the nominal parameter set. Even if *ad-hoc* controllers could be developed to gain command in such circumstances, the focus here was once again on comparing both vehicle architectures under the same conditions.

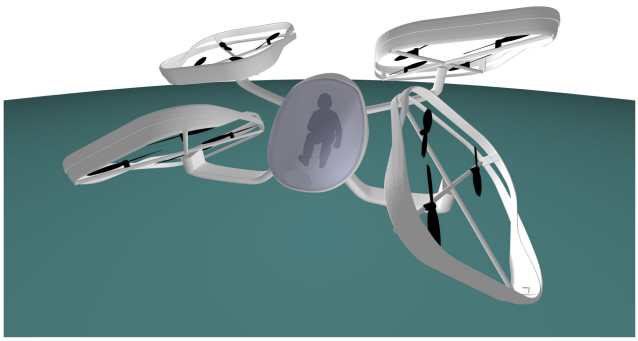

FIGURE 11. The control algorithm is capable of finding nontrivial configurations to overcome a propeller loss and stabilize the system.

In the case of the fully actuated architecture, losing a rotor implies the inability to further control the full orientation of the corresponding rotor module. However, Figure 11 shows how, making use of the linear controller developed in previous sections, the rest of rotor modules get to rearrange and compensate resulting forces and moments.

Figure 12 shows a comparison of the cabin states of both vehicle architectures reacting to a rotor failure at time $t_f = 2$ s. Stationary error is due to the divergence between the real system and the nominal model of the system used

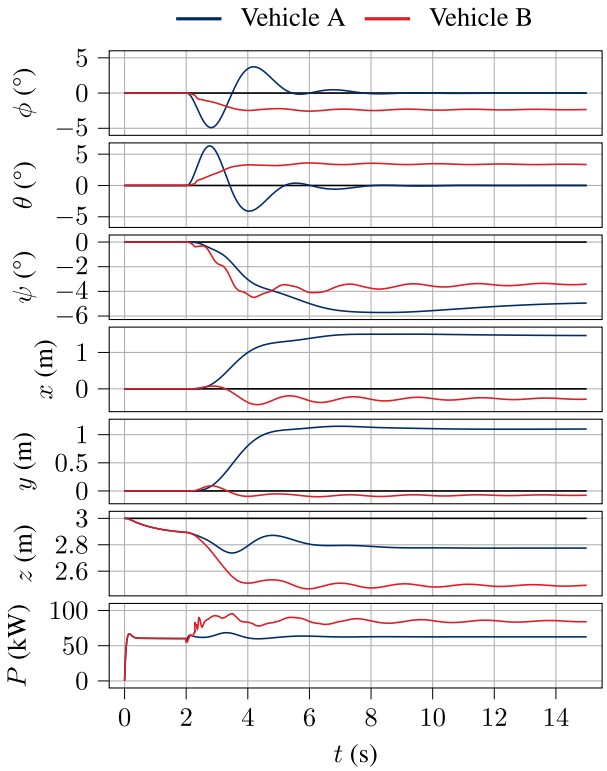

FIGURE 12. Cabin states reacting to a propeller loss with nominal controller parameter set.

to develop the control law, which does not consider the rotor failure, it could be improved adding an integral term to the controller or switching to a different control law that explicitly takes into consideration the dynamics of the new situation.

With the current control strategy, model A shows better stabilization of angular position error. Nevertheless, both vehicles are able to regain control and safely perform an emergency landing. It should be noted that reducing the universal joint range would lead to a smaller increase in consumed power for vehicle B.

V. CONCLUSION

In this work, a comparative analysis between two VTOL multirotor vehicle architectures in common UAM scenarios has been presented: a conventional parallel axis underactuated vehicle and an overactuated vehicle with a passive rotor tilting mechanism based on universal joints. The comparison shows that, when controlled with linear controllers optimized with respect to equivalent cost functions, the overactuated vehicle is capable of achieving greater performance in terms of stability, efficiency, precision and passenger comfort.

Besides, both vehicles have shown capability to overcome a rotor failure situation, providing the required safety. Even if the overactuated vehicle presents improvements in nominal performance, it comes at the expense of worse performance in degraded mode after a rotor failure. Nevertheless, the overactuated vehicle is capable of guaranteeing stability and a safe landing.

Future work could include the analysis of trajectory tracking controllers and forward flight operation, where the influence of drag on the cabin is likely to affect energy consumption: overactuated vehicles are capable of maintaining the cabin at the minimum drag configuration, while underactuated multirotors must constantly adjust cabin orientation, affecting drag and power consumption.

ACKNOWLEDGMENT

The authors would like to thank Alexandre Paris and Leire Abad for providing the graphical design of the air taxi, Arkaitz Oyarzabal for his help determining inertial parameters by means of CAD software and Iñigo Eguizabal for his useful knowledge on power train component selection. Besides, the authors are grateful to Russ Tedrake and the Drake development team for providing high quality open source resources.

REFERENCES

[1] D. Duwe, L. Keicher, P. Ruess, and F. Klausmann, "Quo vadis 3d mobility. technological readiness, urban and rural use cases & urban integration of flying cars and passenger drones," *Fraunhofer IAO*, 2019. [Online]. Available: http://publica.fraunhofer.de/documents/N-569614.html

[2] M. Hamandi, F. Usai, Q. Sablé, N. Staub, M. Tognon, and A. Franchi. (Jan. 2020). *Survey on Aerial Multirotor Design: A Taxonomy Based on Input Allocation*. [Online]. Available: https://hal.archives-ouvertes.fr/hal-02433405

[3] B. Crowther, A. Lanzon, M. Maya-Gonzalez, and D. Langkamp, "Kinematic analysis and control design for a nonplanar multirotor vehicle," *J. Guid., Control, Dyn.*, vol. 34, no. 4, pp. 1157–1171, 2011, doi: 10.2514/1.51186.

[4] G. Jiang and R. Voyles, "Hexrotor UAV platform enabling dextrous interaction with structures-flight test," in *Proc. IEEE Int. Symp. Saf., Secur., Rescue Robot. (SSRR)*, Oct. 2013, pp. 1–6, doi: 10.1109/SSRR.2013.6719377.

[5] S. Rajappa, M. Ryll, H. H. Bulthoff, and A. Franchi, "Modeling, control and design optimization for a fully-actuated hexarotor aerial vehicle with tilted propellers," in *Proc. IEEE Int. Conf. Robot. Autom. (ICRA)*, May 2015, pp. 4006–4013, doi: 10.1109/ICRA.2015.7139759.

[6] M. Ryll, G. Muscio, F. Pierri, E. Cataldi, G. Antonelli, F. Caccavale, and A. Franchi, "6D physical interaction with a fully actuated aerial robot," in *Proc. IEEE Int. Conf. Robot. Autom. (ICRA)*, May 2017, pp. 5190–5195, doi: 10.1109/icra.2017.7989608.

[7] A. Nikou, G. C. Gavridis, and K. J. Kyriakopoulos, "Mechanical design, modelling and control of a novel aerial manipulator," in *Proc. IEEE Int. Conf. Robot. Autom. (ICRA)*, May 2015, pp. 4698–4703, doi: 10.1109/ICRA.2015.7139851.

[8] S. Park, J. Lee, J. Ahn, M. Kim, J. Her, G.-H. Yang, and D. Lee, "ODAR: Aerial manipulation platform enabling omnidirectional wrench generation," *IEEE/ASME Trans. Mechatronics*, vol. 23, no. 4, pp. 1907–1918, Aug. 2018, doi: 10.1109/TMECH.2018.2848255.

[9] D. Brescianini and R. D'Andrea, "An omni-directional multirotor vehicle," *Mechatronics*, vol. 55, pp. 76–93, Nov. 2018, doi: 10.1016/j.mechatronics.2018.08.005.

[10] M. Ryll, D. Bicego, and A. Franchi, "Modeling and control of FAST-hex: A fully-actuated by synchronized-tilting hexarotor," in *Proc. IEEE/RSJ Int. Conf. Intell. Robots Syst. (IROS)*, Oct. 2016, pp. 1689–1694, doi: 10.1109/IROS.2016.7759271.

[11] M. Ryll, H. H. Bulthoff, and P. R. Giordano, "A novel overactuated quadrotor unmanned aerial vehicle: Modeling, control, and experimental validation," *IEEE Trans. Control Syst. Technol.*, vol. 23, no. 2, pp. 540–556, Mar. 2015, doi: 10.1109/tcst.2014.2330999.

[12] A. Oosedo, S. Abiko, S. Narasaki, A. Kuno, A. Konno, and M. Uchiyama, "Flight control systems of a quad tilt rotor unmanned aerial vehicle for a large attitude change," in *Proc. IEEE Int. Conf. Robot. Autom. (ICRA)*, May 2015, pp. 2326–2331, doi: 10.1109/icra.2015.7139508.

[13] M. Kamel, S. Verling, O. Elkhatib, C. Sprecher, P. Wulkop, Z. Taylor, R. Siegwart, and I. Gilitschenski, "The voliro omniorientational hexacopter: An agile and maneuverable tiltable-rotor aerial vehicle," *IEEE Robot. Autom. Mag.*, vol. 25, no. 4, pp. 34–44, Dec. 2018, doi: 10.1109/MRA.2018.2866758.

[14] M. Odelga, P. Stegagno, and H. H. Bulthoff, "A fully actuated quadrotor UAV with a propeller tilting mechanism: Modeling and control," in *Proc. IEEE Int. Conf. Adv. Intell. Mechatronics (AIM)*, Jul. 2016, pp. 306–311, doi: 10.1109/AIM.2016.7576784.

[15] M. Nigro, F. Pierri, and F. Caccavale, "Preliminary design, modeling and control of a fully actuated quadrotor UAV," in *Proc. Int. Conf. Unmanned Aircr. Syst. (ICUAS)*, Jun. 2019, pp. 1108–1116, doi: 10.1109/ICUAS.2019.8798092.

[16] N. Michael, J. Fink, and V. Kumar, "Cooperative manipulation and transportation with aerial robots," *Auto. Robots*, vol. 30, no. 1, pp. 73–86, Jan. 2011, doi: 10.1007/s10514-010-9205-0.

[17] R. Ritz, M. W. Müller, M. Hehn, and R. D'Andrea, "Cooperative quadrocopter ball throwing and catching," in *Proc. IEEE/RSJ Int. Conf. Intell. Robots Syst.*, Oct. 2012, pp. 4972–4978, doi: 10.1109/IROS.2012.6385963.

[18] H.-N. Nguyen, S. Park, J. Park, and D. Lee, "A novel robotic platform for aerial manipulation using quadrotors as rotating thrust generators," *IEEE Trans. Robot.*, vol. 34, no. 2, pp. 353–369, Apr. 2018, doi: 10.1109/TRO.2018.2791604.

[19] A. Tagliabue, M. Kamel, R. Siegwart, and J. Nieto, "Robust collaborative object transportation using multiple MAVs," *Int. J. Robot. Res.*, vol. 38, no. 9, pp. 1020–1044, Aug. 2019, doi: 10.1177/0278364919854131.

[20] I. Iriarte, E. Otaola, D. Culla, I. Iglesias, J. Lasa, and B. Sierra, "Modeling and control of an overactuated aerial vehicle with four tiltable quadrotors attached by means of passive universal joints," in *Proc. Int. Conf. Unmanned Aircr. Syst. (ICUAS)*, Sep. 2020, pp. 1748–1756, doi: 10.1109/ICUAS48674.2020.9213848.

[21] S. Bouabdallah, "Design and control of quadrotors with application to autonomous flying," Ph.D. dissertation, Lab. de Sistèmes Autonomes, École Polytechn. Fédérale de Lausanne, Lausanne, Switzerland, 2007, doi: 10.5075/epfl-thesis-3727.

[22] R. Featherstone, *Rigid Body Dynamics Algorithms*. Boston, MA, USA: Springer, 2014, doi: 10.1007/978-1-4899-7560-7.

[23] R. Tedrake and T. D. D. Team. (2019). *Drake: Model-based design and verification for robotics*. [Online]. Available: https://drake.mit.edu

[24] R. Deits. (2021). *Meshcat*. [Online]. Available: https://github.com/rdeits/meshcat

[25] R. Tedrake. (2010). *Underactuated Robotics: Algorithms for Walking, Running, Swimming, Flying, and Manipulation*. [Online]. Available: http://underactuated.mit.edu

[26] S. M. LaValle, *Planning Algorithms*. Cambridge, U.K.: Cambridge Univ. Press, 2006.

[27] M. A. Sherman, A. Seth, and S. L. Delp, "Simbody: Multibody dynamics for biomedical research," *Procedia IUTAM*, vol. 2, pp. 241–261, Dec. 2011, doi: 10.1016/j.piutam.2011.04.023.

[28] D. Shi, X. Dai, X. Zhang, and Q. Quan, "A practical performance evaluation method for electric multicopters," *IEEE/ASME Trans. Mechatronics*, vol. 22, no. 3, pp. 1337–1348, Jun. 2017, doi: 10.1109/TMECH.2017.2675913.

[29] H. M. Reynolds. (1978). *The Inertial Properties of the Body and its Segments*. [Online]. Available: https://ntrs.nasa.gov/citations/19790003563

[30] K. Cole, "Reactive trajectory generation and formation control for groups of UAVs in windy environments," Ph.D. dissertation, School Eng. Appl. Sci., The George Washington University, Washington, DC, USA, 2018. [Online]. Available: https://scholarspace.library.gwu.edu/etd/bn9997056

[31] J. L. Moore, "Robust post-stall perching with a fixed-wing uav," Ph.D. dissertation, Dept. Mech. Eng., Massachusetts Inst. Technol., Cambridge, MA, USA, 2014. [Online]. Available: http://hdl.handle.net/1721.1/93861

[32] E. Branlard, "Wind energy: On the statistics of gusts and their propagation through a wind farm," *ECN Wind Memo*, vol. 7, pp. 5–9, Oct. 2009.

[33] D. P. Bertsekas, *Dynamic Programming and Optimal Control*, vol. 1. Belmont, MA, USA: Athena Scientific, 1995.

[34] A. E. Bryson, *Applied Optimal Control: Optimization, Estimation and Control*. Boca Raton, FL, USA: CRC Press, 1975.

[35] M. W. Mueller and R. D'Andrea, "Stability and control of a quadrocopter despite the complete loss of one, two, or three propellers," in *Proc. IEEE Int. Conf. Robot. Autom. (ICRA)*, May 2014, pp. 45–52, doi: 10.1109/ICRA.2014.6906588.

[36] M. Frangenberg, J. Stephan, and W. Fichter, "Fast actuator fault detection and reconfiguration for multicopters," in *Proc. AIAA Guid., Navigat., Control Conf.*, Jan. 2015, p. 1766, doi: 10.2514/6.2015-1766.

IMANOL IRIARTE received the B.S. and M.S. degrees in mechatronics from the Public University of Navarre, Spain, in 2016 and 2018, respectively. He is currently pursuing the Ph.D. degree with the Tecnalia Research and Innovation, Spain, in collaboration with the University of the Basque Country, Spain. Both Bachelor and Master theses were elaborated and presented at the Technische Universität Darmstadt, Germany. His main research interests include dynamics, optimization and control, and their application to aerial robotics and urban air mobility.

IÑAKI IGLESIAS received the B.S. degree in materials engineering from TECNUN, San Sebastián, Spain, in 2002, and the M.S. degree in mechanical engineering from the University of the Basque Country (UPV/EHU), Bilbao, Spain, in 2013. He is currently a Principal Technologist with the Electric Aircraft Lab, Tecnalia Research and Innovation, and leads the research about aircraft electrification and new electric architectures. His research interests include modeling and simulation of complex systems, and design and control of non-conventional multicopter architectures.

JOSEBA LASA received the M.Sc. degree from Tecnun, Donostia-San Sebastián, Spain, in 2001, and the Ph.D. degree from the University of the Basque Country, Bilbao, Spain, in 2012, both in mechanical engineering. He is currently the Director of the Electric Aircraft Lab, Tecnalia Research and Innovation, Donostia-San Sebastian. His main research interests include aircraft electrification, strategic foresight, and product design.

HODEI CALVO-SORALUZE received the B.S. degree in physics from the University of the Basque Country (UPV/EHU), Leioa, Spain, in 2016, and the M.S. degree in computational engineering and intelligent systems, UPV/EHU, San Sebastián, Spain, in 2018. He is currently pursuing the Ph.D. degree with the Tecnalia Research and Innovation, in collaboration with UPV/EHU. His main research interests include machine learning, deep learning, and their multiple applications, such as urban air mobility and robotics.

BASILIO SIERRA is currently a Full Professor with the Department of Computer Sciences and Artificial Intelligence, University of the Basque Country. He is the Co-Director of the Robotics and Autonomous Systems Group, Donostia-San Sebastian. He is also a Researcher in the fields of robotics and machine learning, where he is working on the use of different paradigms to improve behaviours. His research interests include machine learning, data analysis, computer vision, and robotics.